

Sign reversal of Berry curvature triple driven by magnetic phase transition in a ferromagnetic polar metal

Xuyang Sha^{1,2,†}, Xuejin Zhang^{3,†}, Hao Liu^{1,2,†}, Jin Cao³, Ruohan Chen², Jinfeng Zhai^{1,2},
Dingfu Shao⁴, Shiwei Wu^{1,2}, Cong Xiao^{5*}, Shengyuan A. Yang^{3*}, Pan He^{1,6,7*},
Hangwen Guo^{1,6,7*} and Jian Shen^{1,2,6,7,8*}

¹ *State Key Laboratory of Surface Physics and Institute for Nanoelectronic Devices and Quantum Computing, Fudan University, Shanghai 200433, China*

² *Department of Physics, Fudan University, Shanghai 200433, China*

³ *Institute of Applied Physics and Materials Engineering, Faculty of Science and Technology, University of Macau, Macau, China*

⁴ *Key Laboratory of Materials Physics, Institute of Solid State Physics, HFIPS, Chinese Academy of Sciences, Hefei 230031, China*

⁵ *Interdisciplinary Center for Theoretical Physics and Information Sciences (ICTPIS), Fudan University, Shanghai 200433, China*

⁶ *Shanghai Research Center for Quantum Sciences, Shanghai 201315, China*

⁷ *Zhangjiang Fudan International Innovation Center, Fudan University, Shanghai 201210, China*

⁸ *Collaborative Innovation Center of Advanced Microstructures, Nanjing 210093, China*

Abstract

Nonlinear Hall effects have been observed in quantum materials where Berry curvature and its momentum-space derivatives, such as the Berry curvature dipole (BCD) and Berry curvature triple (BCT), play a central role. While inversion symmetry breaking is widely recognized as a key criterion, the impact of time-reversal symmetry breaking remains less explored. Here, we report an abrupt enhancement of nonlinear Hall conductivity in non-centrosymmetric SrRuO₃ (111) thin films during the paramagnetic-to-ferromagnetic transition. Scaling analysis reveals a sign reversal of the skew scattering contribution upon time-reversal symmetry breaking, which we attribute to the sign reversal of BCT at the Fermi surface. Density functional theory (DFT) calculations support this interpretation, showing the spin-polarized band splitting shifts the Fermi level asymmetrically for different spin channels. Our findings establish SrRuO₃ (111) thin films as a promising platform for exploring magnetically tunable nonlinear transport effects.

The interplay between magnetism and Berry curvature has emerged as a key factor in understanding exotic transport phenomena in magnetic systems [1,2]. In ferromagnets with spin-orbit coupling, the magnetic phase transitions lift spin degeneracy. Along with the spin-orbit coupling induced nodal structure [3,4], it significantly modify the band structure and Berry curvature distributions, leading to transport phenomena such as anomalous Hall effect [5,6] and topological Hall effect [7,8]. Beyond these linear Hall responses, nonlinear Hall effect (NHE) has attracted significant attention in recent years. It has been widely observed at zero magnetic field in non-magnetic systems that break spatial inversion symmetry while preserving time-reversal symmetry [9–12]. The nonlinear transport properties are deeply rooted in the Berry curvature and its momentum-space derivatives, such as the Berry curvature dipole (BCD) and Berry curvature triple (BCT) [13–15]. Studying these quantities in ferromagnetic system is of great interest since the spontaneous magnetization can fundamentally modifies the Berry curvature landscape, enabling magnetization-tunable nonlinear Hall responses. Such exploration can pave the way for leveraging nonlinear responses in spintronics where control over spin-dependent nonlinear transport is highly desirable [9,16].

Despite its importance, investigation of NHE in ferromagnetic systems remains limited, as most conventional ferromagnets possess centrosymmetric structure. Itinerant electrons in ferromagnetic metals can effectively screen local dipole moments, suppressing spontaneous inversion symmetry breaking [17–19]. As a result, the inherent symmetry constraints pose significant challenges in detecting and realizing

nonlinear transport phenomena in ferromagnetic materials. Complex oxides offer new opportunities for this purpose where strong charge-spin-lattice coupling enables the engineering of structural, electronic, and magnetic properties, and allows control over spatial-inversion and time-reversal symmetry [20–23]. Remarkably, strain engineering in ferromagnetic metallic oxides can induce electrical polarity, stabilizing a magnetic polar metal phase [8,24–26]. Such phase naturally breaks both spatial-inversion and time-reversal symmetry, creating an ideal platform to investigate the nonlinear transport effects in ferromagnets.

In this work, we report the observation of nonlinear Hall effect in ferromagnetic polar metal SrRuO₃ (111) thin films, which exhibit inversion symmetry breaking by flexoelectric effect [27]. During the paramagnetic-to-ferromagnetic phase transition at 138K, we observed a large enhancement of nonlinear Hall conductivity. Remarkably, the scaling law analysis suggests that when the time-reversal symmetry is broken, the skew scattering contribution induced by the BCT reverses its sign. DFT calculations suggest that the sign reversal can be attributed to the splitting of spin-polarized bands in the ferromagnetic phase, which induces a sign reversal in BCT. Our observations shed lights on nonlinear transport behavior in ferromagnetic systems.

SrRuO₃ (111) thin films were grown on SrTiO₃ (111) substrate via pulsed laser deposition technique (See methods for details). As shown in Figure 1a, standard Hall bar devices were fabricated via photolithography for transport measurements. The first ($V^{1\omega}$) and second order harmonic voltages ($V^{2\omega}$) can be obtained under an ac source current $I_x = I \sin \omega t$ using lock-in techniques. Figure 1b shows the longitudinal

resistivity ρ_{xx} as function of temperature for the thin film with 8 nm thickness. The film shows typical metallic behavior as the ρ_{xx} monotonically decreases with lowering temperature. A kink at 138 K indicates the paramagnet to ferromagnet phase transition. To further verify the transition, we measured anomalous Hall effect at different temperatures. We plot the Hall resistivity ρ_{xy} as function of out-of-plane magnetic field for several representative temperatures in Fig. 1c. Above 138 K, the anomalous Hall effect is negligible indicating the absence of magnetic order. Below 138 K, the anomalous Hall signal start to emerge and exhibit hysteresis behavior, consistent with the ferromagnetic metal properties reported in SrRuO₃ thin films [6,28,29]. ρ_{xy} has a very small contribution from the contact misalignment of the Hall bar devices (Supplementary Figure S1).

Strain gradient due to heteroepitaxy can induce non-centrosymmetric structure that breaks inversion symmetry [30]. In SrRuO₃ (111) thin film, recent observation shows that shear strain gradient causes large Ru ion off-centering displacement along [-1-10] direction, as illustrated in Figs 1e and 1f [27]. Such displacement gives rise to a non-centrosymmetric polar structure. To examine the existence, we performed optical second-harmonic generation (SHG) and the results are shown in Figure 1d. Threefold symmetric SHG anisotropy pattern is observed which aligns well with point group m with three equivalent electric dipoles originated from 120° rotated domains as illustrated in Figure 1e, and in good agreement with previous report [31]. These results confirm the emergence of inversion-symmetry breaking in a ferromagnetic metallic system, offering a rare breed to explore NHE under time-reversal symmetry breaking

conditions.

Figure 2a shows the second-harmonic transverse voltage $V_y^{2\omega}$ measured in zero magnetic field at room temperature. $V_y^{2\omega}$ shows quadratic current dependence (i.e. $V_y^{2\omega} \propto I^2$) and changes sign when reversing the current and corresponding Hall probe directions, validating the nonlinear origin. We further verified that $V_y^{2\omega}$ signal is independent of the ac frequency used (Supplementary Figure S2), suggesting negligible capacitive contributions. These results unambiguously illustrate the existence of transverse nonlinear transport in SrRuO₃ (111) thin film and are in line with its inversion-symmetry breaking nature [27,31]. We then investigate the temperature dependence of transverse nonlinear transport properties. Figure 2b shows the $V_y^{2\omega} \sim I^2$ curve at different temperatures under zero magnetic field, all of which shows good quadratic current dependence. The slope of the $V_y^{2\omega} \sim I^2$ curves is defined as the 2nd order Hall resistance R_{yxx} , which is plotted along with the ρ_{xx} in Figure 2c. In the paramagnetic phase, R_{yxx} shows a monotonic decrease following a similar trend with ρ_{xx} . Interestingly, when entering the ferromagnetic phase transition, an abrupt enhancement of R_{yxx} is clearly observed. The anomalous change in nonlinear Hall effect should be due to time-reversal symmetry breaking. Here, we carefully examined and excluded the contribution of anomalous Nernst effect, which may exist under time-reversal symmetry breaking [32–37] (see supplementary note 1 and Figure S3). Similar enhancement is also observed in a thick 25nm film, further validating that such behavior does not originate from surface or interface, but rather reflects intrinsic nonlinear physics during the magnetic phase transition (supplementary Figure S4).

To gain more insight into the effect of time-reversal symmetry breaking, we calculate the nonlinear transverse conductivity $\sigma_{yxx}^{(2)} = \sigma_{xx} \frac{V_y^{2\omega} L^2}{(V_x^\omega)^2 W}$ during the paramagnetic-to-ferromagnetic phase transition, where L and W are the length and width of the Hall bar channel. The results are shown in Figure 3a. While $\sigma_{yxx}^{(2)}$ remains nearly unchanged above T_c , a sharp increase of $\sigma_{yxx}^{(2)}$ is clearly observed in the ferromagnetic phase. We then analyze the scaling behavior to identify the microscopic origins [10,14]. Using the temperature-dependent data, $\sigma_{yxx}^{(2)}/\sigma_{xx}$ is plotted as a function of σ_{xx}^2 as shown in Figure 3b. Such analysis can effectively separate different contributions to the transverse nonlinear transport according to the scaling laws $\sigma_{yxx}^{(2)} = \xi\sigma_{xx}^3 + \eta\sigma_{xx}$. According to Drude model, in the low frequency limit, the longitudinal conductivity can be approximated as $\sigma_{xx} \propto \tau$ [38]. ξ and η represent the contributions of τ^3 and τ respectively. Specifically, a linear fitting should be expected where the slope ξ corresponds to the τ^3 contribution to the $\sigma_{yxx}^{(2)}$ that comes from skew scattering, and the interception η corresponds to a τ contribution to $\sigma_{yxx}^{(2)}$ that originates from Berry curvature dipole (BCD) or side jump [10,14]. Considering that the system has general three-fold symmetry suggested by the results in Fig. 1d, the contribution of BCD is negligible [39]. Furthermore, the second-order conductivity contributed by skew scattering can be expressed as $\sigma^{(2),sk} \approx \frac{e^3 v_F \tau^3}{\hbar^2 \tilde{\tau}}$ [14,40]. $\tilde{\tau}$ is the skew scattering time, which is proportional to BCT under three-fold symmetry, $\tilde{\tau} \propto \text{BCT}$. From Figure 3b, two distinct regimes are clearly observed, which are corresponding to the paramagnetic ($\sigma_{xx}^2 < 16 \times 10^6 \text{ (S/cm)}^2$) and ferromagnetic ($\sigma_{xx}^2 > 16 \times 10^6 \text{ (S/cm)}^2$) phases, respectively. Both regimes show good

linear fittings consistent with the scaling behavior discussed. We extracted the ξ values from the fittings, which represent the skew scattering contribution. An interesting finding is that ξ experiences a sign change during the paramagnetic-to-ferromagnetic transition. Such scaling behavior is cross-checked in another sample (Supplementary Figure S5), validating our experimental results and analysis. Moreover, from temperature-dependent SHG measurements (Supplementary Figure S7) [41], we do not observe any structural change or non-collinear magnetic inhomogeneity during the magnetic phase transition, pointing towards electronic band contribution as the origin of our observation.

We then explore the sign change of the skew scattering contribution from first-principles calculations. As mentioned, in a system with threefold rotation symmetry, the skew scattering strength can be measured by BCT [13–15]: $\text{BCT}(\mu) = 2\pi\hbar \int \frac{d\mathbf{k}}{(2\pi)^2} \delta(\varepsilon_{\mathbf{k}} - \mu) \Omega_z(\mathbf{k}) \cos 3\theta_{\mathbf{k}}$, which integrates the Berry curvature $\Omega_z(\mathbf{k})$ over the Fermi surface, and $\theta_{\mathbf{k}}$ is the angular coordinate, as illustrated in Fig. 4a. The structure of the SrRuO₃ (111) surface is shown in Fig. 4a. It exhibits inversion symmetry along with threefold rotational and mirror symmetries, as indicated by the dashed lines. The combined \mathcal{PT} symmetry enforces double degeneracy in the band structure, leading to a vanishing Berry curvature and consequently a zero BCT. However, the \mathcal{PT} symmetry is broken when an SrRuO₃ thin film is grown on an SrTiO₃ (111) substrate. In this case, a shear strain is imposed on the SrRuO₃, resulting in a flexo-polar phase, as evidenced by scanning transmission electron microscopy. It was observed that the Ru atoms undergo an off-center shift along [110] direction by 0.1 Å on average. This

displacement results in a polar domain with reduced symmetry, leaving only a single mirror. As shown in Fig. 4a, there are three equivalent domains in which the Ru atoms are off centering along $[110]$, $[101]$, and $[011]$ directions, respectively. These polar domains are related by C_{3z} , and the overall system retains C_{3z} symmetry while inversion symmetry remains broken. It should be noted the electrons on Fermi surface are mainly derived from Ru atoms. The off-centering Ru atoms shall significantly alter the transport properties of SrRuO₃ thin film.

To model the flexo-polar phase with three equivalent domains, in the first-principles calculations we directly shift the Ru atoms along the $[111]$ direction, instead of the realistic displacements as given in Fig. 4a. The resulting structure breaks inversion symmetry, but preserves the threefold axis C_{3z} , which is in line with our SHG result. Meanwhile, this choice captures the C_{3z} symmetry of the skew scattering process as electron travels through the ensemble of domains. We set the displacement of 0.1 \AA , which was selected based on the previous report. We first examine the nonmagnetic phase above the critical temperature. Due to \mathcal{PT} symmetry breaking, there is a band splitting of approximately 40 meV on the Fermi surface, as shown in Fig. 4b. Such a small splitting originates from the spin-orbit coupling. It enables sizable Berry curvature distributions as shown in Fig. 4c, which respects C_{3z} . In contrast, in the ferromagnetic phase below the critical temperature, the band splitting is significantly larger than in the nonmagnetic case, as it originates from the exchange interaction, and the magnetization is primarily associated with Ru atoms. The large band splitting is also evident in the Fermi surface shown in Fig. 4e, which reveals a

very different pattern of Berry curvature. We then calculated the BCT in both nonmagnetic and ferromagnetic phases. As shown in Fig. 4f, across a broad energy window around the chemical potential, the BCT exhibits opposite signs in the two phases. This result is consistent with our observed sign reversal of the skew scattering contribution near the phase transition temperature. Moreover, our first-principles results indicate that this sign reversal originates from the distinct mechanisms generating Berry curvature in the two phases (spin-orbit gap versus exchange gap).

In summary, we report an abrupt change of nonlinear transverse transport in polar metal SrRuO₃(111) film during the paramagnetic-to-ferromagnetic transition. This phenomenon is attributed to the sign reversal of Berry curvature triple (BCT) driven by the magnetic phase transition. Our results not only open the door to explore nonlinear transport phenomena in ferromagnetic systems but also provide opportunity to engineer nonlinear responses in magnetic oxides for spintronic devices.

Methods

Sample Fabrication and characterization. SrRuO₃ thin films were grown on SrTiO₃(111) substrates using a pulsed-laser deposition system with a KrF excimer laser (248nm). Before deposition, SrTiO₃ substrates (miscut <0.1°) were etched with a buffered hydrofluoric acid solution and then annealed in air at 1,050 °C for 1 h to produce an atomically flat surface with a unit-cell step terrace structure. During deposition, the temperature of the substrate was maintained at 650° C and SrRuO₃ films were grown under an oxygen pressure of 80 mTorr with a laser fluence of 2 J cm⁻² and a frequency of 5Hz. A high-pressure reflection high-energy electron diffraction system was used to monitor the growth. A smooth surface is observed as shown in Supplementary Figure S8, which is further confirmed by Atomic force microscopy (Park NX10 with Al-coated tips). X-ray diffraction Φ scan was performed using a Bruker D8 Discover system.

Device fabrication. Conventional photolithography and ion beam etching were used to pattern the SrRuO₃ films into the Hall bar geometry. The channel size was minimized to 50 × 187.5 μm². After patterning, the samples were ex-situ annealed at 300 ° C in ambient oxygen flow for 3 h to minimize the oxygen deficiency induced during growth and ion-milling. Cr (5 nm) and Au (60 nm) films were sputtered onto the Hall bar as contact electrodes. After the entire fabrication process, the SRO conducting channels still exhibit atomically-flat topography (Supplementary Figure S8).

Electric transport measurements. The transport data were measured using a physical properties measurement system (PPMS, Quantum Design). We performed low-frequency ac electric harmonic measurements using Keithley current source (6221) and Stanford Research lock-in amplifiers (SR830). During the measurements, a sinusoidal current with a frequency $f = \omega/2\pi = 17.3$ Hz is applied to the devices, and the in-phase (0°) first harmonic voltage V^ω and out-of-phase (90°) second harmonic voltage $V^{2\omega}$ along the longitudinal and transverse voltages were measured simultaneously by four lock-in amplifiers.

Optical second harmonic generation measurements.

The nonlinear SHG measurements were conducted in a variable-temperature optical cryostat housed inside a superconducting magnet with a room-temperature bore. The excitation beam (120 fs, 80 MHz, 820 nm) from a Ti:sapphire oscillator (MaiTai HP, Spectra Physics) was focused onto the sample at normal incidence using a 50× microscopic objective (NA = 0.55). The reflected nonlinear optical signal was collected by the same objective and detected by either a photomultiplier tube in photon-counting mode or a spectrograph equipped with a liquid-nitrogen-cooled charge coupled device. To measure the polarization-resolved intensity of nonlinear optical signal, the polarization of the excitation and signal beams was rotated with respect to the sample simultaneously using a half-wave plate. The polarization state of the signal beam was analyzed by a linear polarizer placed in front of detectors. For the measurements of temperature dependence and magnetic hysteresis loops, the excitation beam was circularly polarized using a quarter-wave plate.

Computational details.

The first-principles calculations were performed using the Vienna Ab initio Simulation Package. The projector-augmented wave method was employed to describe the interactions between ions and electrons. Exchange-correlation effects were treated self-consistently using the Perdew-Burke-Ernzerhof functional. The cutoff energy was set to be 500 eV. The Brillouin zone was sampled by a k -point grid of $9 \times 9 \times 9$. The convergence threshold for energy and force were set to 10^{-6} eV and 0.01 eV/Å, respectively. The spin-orbit coupling was considered in all calculations. The *ab initio* tight-binding model was constructed using the Wannier90 package, which was used for calculating the Berry curvature and the BCT.

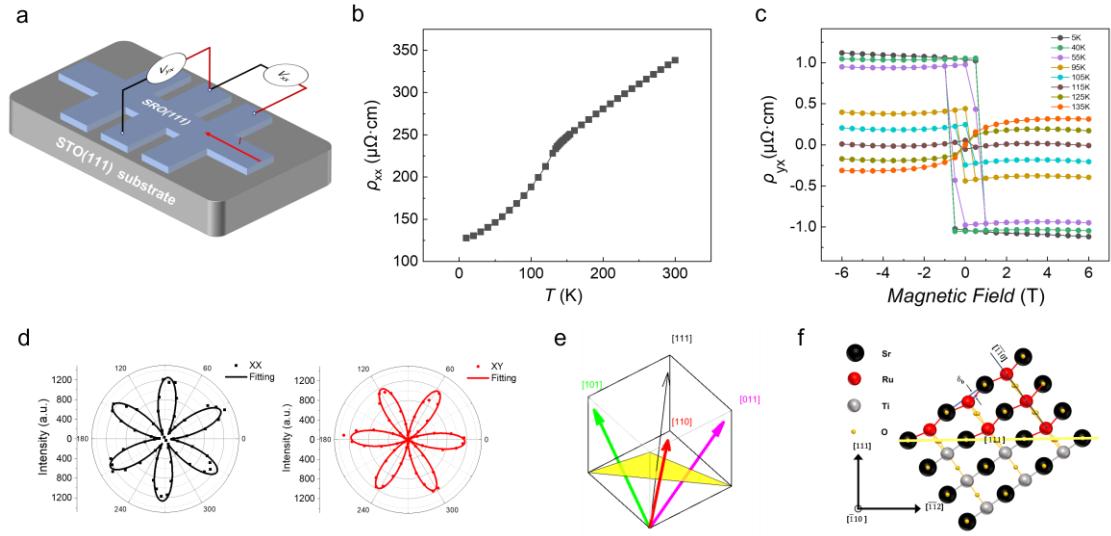


Figure 1. (a) Schematic of hall-bar device of SrRuO₃ thin film. A sinusoidal current I^ω was applied, and the first harmonic $V^{1\omega}$ and second harmonic $V^{2\omega}$ voltages were simultaneously measured along the longitudinal and transverse directions. (b) The longitudinal resistivity ρ_{xx} as a function of temperature. (c) Field-dependent transverse linear Hall resistivities ($\rho_{yx} \sim H$) of 8 nm SrRuO₃ thin film. (d) SHG patterns acquired under XX and XY polarization configurations. Here, the excitation and detection beams were linearly polarized, with XX and XY referring to co- and cross-linearly polarized between the two beams, respectively. (e) Schematic of polar symmetry in SrRuO₃ (111) thin film with three electric dipoles along [101], [011] and [110] directions. (f) Schematic showing the off-centering of Ru atoms along [-1-10] induced by a flexoelectric field [27].

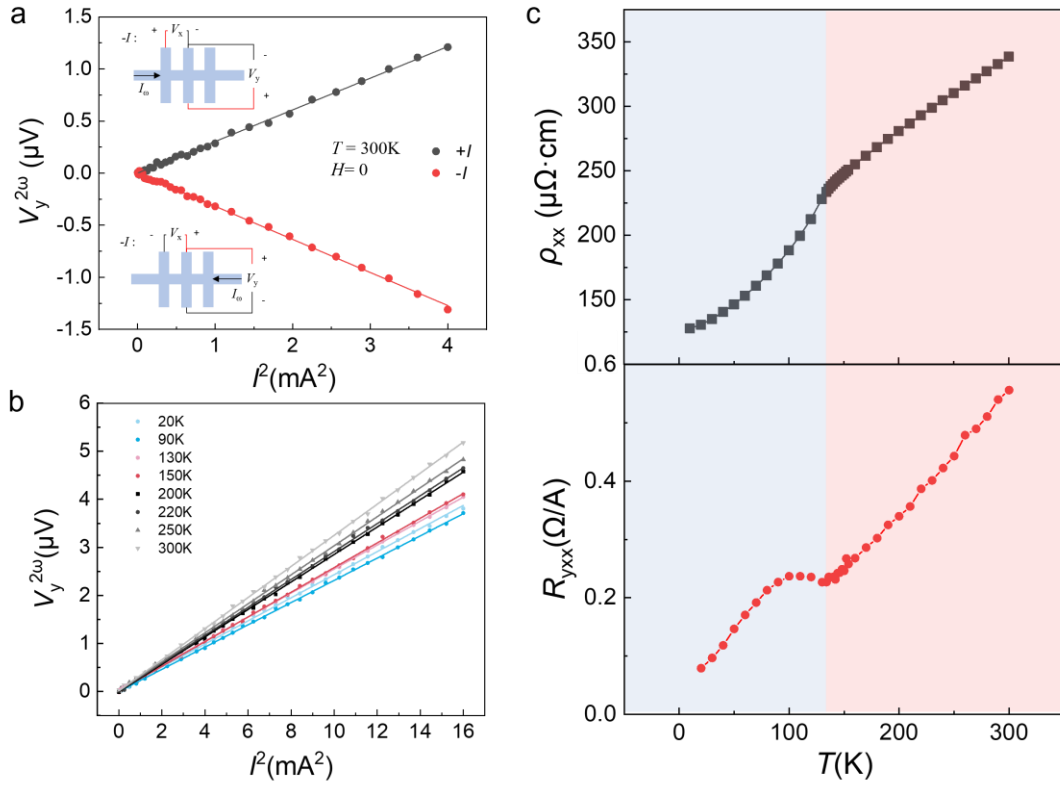


Figure 2. (a) The second-harmonic transverse voltage $V_y^{2\omega}$ versus I^2 for the current along the $[-1-12]$ axis. The solid lines are linear fits to the data. The insets show schematics of current and voltage probe connections under opposite current directions of $+I$ and $-I$. The data were collected at $T = 300$ K without external magnetic field. (b) $V_y^{2\omega}$ versus I^2 at different temperatures, and the slope of which being the nonlinear transverse resistance R_{yxx} . (c) The longitudinal resistivity ρ_{xx} (black) and the nonlinear transverse resistance R_{yxx} (red) versus temperature plotted along. Red and blue regions denote the high temperature paramagnetic and low temperature ferromagnetic phase, respectively.

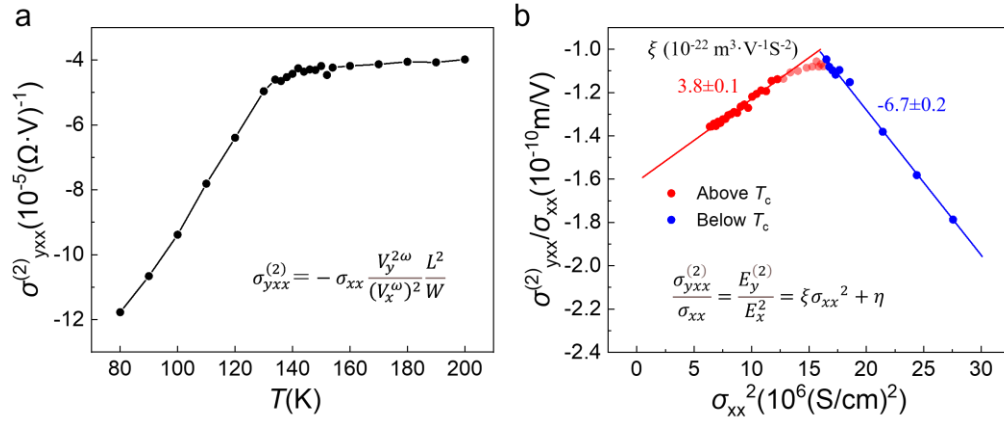


Figure 3. (a) The nonlinear transverse conductivity $\sigma_{yxx}^{(2)}$ as a function of temperature. (b) Scaling law analysis by plotting $\sigma_{yxx}^{(2)} / \sigma_{xx}$ versus σ_{xx}^2 . The dots are the experimental data. The solid lines are linear fits to the experimental data in paramagnetic (red) and ferromagnetic (blue) phases. The slopes ξ of linear fitting for paramagnetic (red) and ferromagnetic (blue) phases are shown.

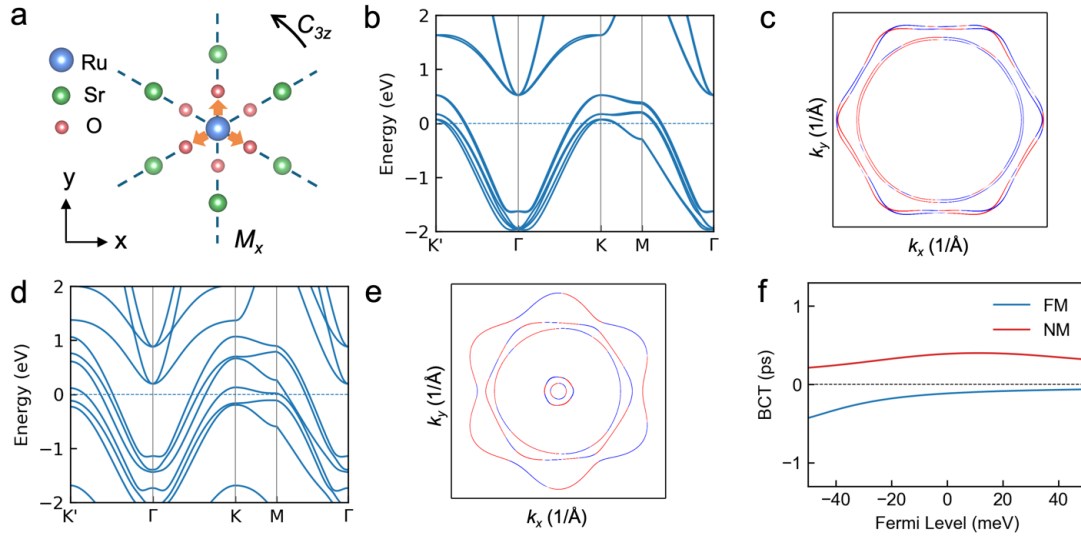


Figure 4. (a) Top view of SrRuO₃ (111). The three vectors represent the displacement of Ru atoms along [110], [101], and [011] for the three polar domains. (b), (c) Calculated band structure and Berry curvature distribution at the Fermi level for the nonmagnetic phase, respectively. (d), (e) Same as (b), (c) but for the ferromagnetic phase. (f) Calculated Berry curvature triple as a function of chemical potential.

References

- [1] D. J. Groenendijk et al., Berry phase engineering at oxide interfaces, *Phys. Rev. Res.* **2**, 023404 (2020).
- [2] D. Xiao, M.-C. Chang, and Q. Niu, Berry phase effects on electronic properties, *Rev. Mod. Phys.* **82**, 1959 (2010).
- [3] K. Kim et al., Large anomalous Hall current induced by topological nodal lines in a ferromagnetic van der Waals semimetal, *Nat. Mater.* **17**, 794 (2018).
- [4] G. Chang et al., Magnetic and noncentrosymmetric Weyl fermion semimetals in the RAlGe family of compounds (R = rare earth), *Phys. Rev. B* **97**, 041104 (2018).
- [5] N. Nagaosa, J. Sinova, S. Onoda, A. H. MacDonald, and N. P. Ong, Anomalous Hall effect, *Rev. Mod. Phys.* **82**, 1539 (2010).
- [6] B. Sohn et al., Sign-tunable anomalous Hall effect induced by two-dimensional symmetry-protected nodal structures in ferromagnetic perovskite thin films, *Nat Mater* **20**, 1643 (2021).
- [7] Q. Qin, L. Liu, W. Lin, X. Shu, Q. Xie, Z. Lim, C. Li, S. He, G. M. Chow, and J. Chen, Emergence of Topological Hall Effect in a SrRuO₃ Single Layer, *Adv. Mater.* **31**, (2019).
- [8] L. Wang et al., Ferroelectrically tunable magnetic skyrmions in ultrathin oxide heterostructures, *Nat Mater* **17**, 1087 (2018).
- [9] Q. Ma et al., Observation of the nonlinear Hall effect under time-reversal-symmetric conditions, *Nature* **565**, 337 (2019).
- [10] K. Kang, T. Li, E. Sohn, J. Shan, and K. F. Mak, Nonlinear anomalous Hall effect in few-layer WTe₂, *Nat Mater* **18**, 324 (2019).
- [11] I. Sodemann and L. Fu, Quantum Nonlinear Hall Effect Induced by Berry Curvature Dipole in Time-Reversal Invariant Materials, *Phys. Rev. Lett.* **115**, 216806 (2015).
- [12] Z. Z. Du, H.-Z. Lu, and X. C. Xie, Nonlinear Hall effects, *Nat. Rev. Phys.* **3**, 744 (2021).

- [13] P. Makushko et al., A tunable room-temperature nonlinear Hall effect in elemental bismuth thin films, *Nat. Electron.* **7**, 207 (2024).
- [14] P. He, H. Isobe, D. Zhu, C. H. Hsu, L. Fu, and H. Yang, Quantum frequency doubling in the topological insulator Bi₂Se₃, *Nat Commun* **12**, 698 (2021).
- [15] J. Zhai, M. Trama, H. Liu, Z. Zhu, Y. Zhu, C. A. Perroni, R. Citro, P. He, and J. Shen, Large Nonlinear Transverse Conductivity and Berry Curvature in KTaO₃ Based Two-Dimensional Electron Gas, *Nano Lett.* **23**, 11892 (2023).
- [16] Y. Zhang and L. Fu, Terahertz detection based on nonlinear Hall effect without magnetic field, *Proc. Natl. Acad. Sci.* **118**, (2021).
- [17] J. Shi et al., Revealing a distortive polar order buried in the Fermi sea, *Sci. Adv.* **10**, (2024).
- [18] S. Bhowal and N. A. Spaldin, Polar Metals: Principles and Prospects, *Annu. Rev. Mater. Res.* **53**, 53 (2023).
- [19] D. Hickox-Young, D. Puggioni, and J. M. Rondinelli, Polar metals taxonomy for materials classification and discovery, *Phys. Rev. Mater.* **7**, 010301 (2023).
- [20] N. A. Benedek and T. Birol, ‘Ferroelectric’ metals reexamined: fundamental mechanisms and design considerations for new materials, *J. Mater. Chem. C* **4**, 4000 (2016).
- [21] T. H. Kim et al., Polar metals by geometric design, *Nature* **533**, 68 (2016).
- [22] Y. Tokura, M. Kawasaki, and N. Nagaosa, Emergent functions of quantum materials, *Nat. Phys.* **13**, 1056 (2017).
- [23] P. V Balachandran, J. Young, T. Lookman, and J. M. Rondinelli, Learning from data to design functional materials without inversion symmetry, *Nat Commun* **8**, 14282 (2017).
- [24] M. Meng et al., Interface-induced magnetic polar metal phase in complex oxides, *Nat Commun* **10**, 5248 (2019).
- [25] J. Zhang et al., A correlated ferromagnetic polar metal by design, *Nat. Mater.* (2024).
- [26] D. Puggioni and J. M. Rondinelli, Designing a robustly metallic noncentrosymmetric ruthenate oxide with large thermopower anisotropy, *Nat*

- Commun **5**, 3432 (2014).
- [27] W. Peng et al., Flexoelectric polarizing and control of a ferromagnetic metal, Nat. Phys. **20**, 450 (2024).
- [28] K. Ni, P. Sharma, J. Zhang, M. Jerry, J. A. Smith, K. Tapily, R. Clark, S. Mahapatra, and S. Datta, Critical Role of Interlayer in Hf_{0.5}Zr_{0.5}O₂ Ferroelectric FET Nonvolatile Memory Performance, IEEE Trans. Electron Devices **65**, 2461 (2018).
- [29] G. Koster, L. Klein, W. Siemons, G. Rijnders, J. S. Dodge, C.-B. Eom, D. H. A. Blank, and M. R. Beasley, Structure, physical properties, and applications of SrRuO₃ thin films, Rev. Mod. Phys. **84**, 253 (2012).
- [30] M. Gu et al., Momentum-space spin texture induced by strain gradient in nominally centrosymmetric SrIrO₃ films, Natl. Sci. Rev. (2023).
- [31] Z. Wang et al., Anomalous strain effect in heteroepitaxial SrRuO₃ films on (111) SrTiO₃ substrates, Chinese Phys. B **31**, (2022).
- [32] Y. S. Lee, J. S. Lee, T. W. Noh, D. Y. Byun, K. S. Yoo, K. Yamaura, and E. Takayama-Muromachi, Systematic trends in the electronic structure parameters of the 4d transition-metal oxides SrMO₃ (M=Zr, Mo, Ru, and Rh), Phys. Rev. B **67**, (2003).
- [33] J. S. Lee, Y. S. Lee, T. W. Noh, K. Char, J. Park, S. J. Oh, J. H. Park, C. B. Eom, T. Takeda, and R. Kanno, Optical investigation of the electronic structures of Y₂Ru₂O₇, CaRuO₃, SrRuO₃, and Bi₂Ru₂O₇, Phys. Rev. B **64**, 245107 (2001).
- [34] J. C. Jiang, W. Tian, X. Q. Pan, Q. Gan, and C. B. Eom, Domain structure of epitaxial SrRuO₃ thin films on miscut (001) SrTiO₃ substrates, Appl. Phys. Lett. **72**, 2963 (1998).
- [35] P. B. Allen, H. Berger, O. Chauvet, L. Forro, T. Jarlborg, A. Junod, B. Revaz, and G. Santi, Transport properties, thermodynamic properties, and electronic structure of SrRuO₃, Phys Rev B Condens Matter **53**, 4393 (1996).
- [36] D. J. Singh, Electronic and magnetic properties of the 4d itinerant ferromagnet SrRuO₃, J. Appl. Phys. **79**, 4818 (1996).

- [37] Y.-L. Wu, G.-H. Zhu, and X.-Q. Yu, Nonlinear anomalous Nernst effect in strained graphene induced by trigonal warping, *Phys. Rev. B* **104**, (2021).
- [38] C. Kittel, *Introduction to Solid State Physics*, 8th ed. (Wiley, New York, 2005).
- [39] H. Liu, J. Zhao, Y. X. Huang, W. Wu, X. L. Sheng, C. Xiao, and S. A. Yang, Intrinsic Second-Order Anomalous Hall Effect and Its Application in Compensated Antiferromagnets, *Phys Rev Lett* **127**, 277202 (2021).
- [40] P. He, G. K. W. Koon, H. Isobe, J. Y. Tan, J. Hu, A. H. C. Neto, L. Fu, and H. Yang, Graphene moire superlattices with giant quantum nonlinearity of chiral Bloch electrons, *Nat Nanotechnol* **17**, 378 (2022).
- [41] Z. Sun et al., Giant nonreciprocal second-harmonic generation from antiferromagnetic bilayer CrI(3), *Nature* **572**, 497 (2019).